Composites Part B 126 (2017) 192–201

Contents lists available at ScienceDirect

Composites Part B

journal homepage: www.elsevier.com/locate/compositesb

# Effect of the fringing electric field on the apparent electric permittivity of cement-based materials

Yulin Wang [a, b], D.D.L. Chung [a, *]

[a] Composite Materials Research Laboratory, Department of Mechanical and Aerospace Engineering, University at Buffalo, The State University of New York, Buffalo, NY 14260-4400, USA

[b] College of Civil Engineering and Architecture, Wuyi University, Wuyi Road 16, Xinfeng street, Wuyi Shan City, Fujian Province 354300, China

ARTICLE INFO

*Article history:*
Received 11 January 2017
Received in revised form
28 May 2017
Accepted 28 May 2017
Available online 29 May 2017

*Keywords:*
Particle-reinforcement
Smart materials
Electrical properties
Non-destructive testing

ABSTRACT

The fringing electric field increases the apparent relative permittivity of cement when the electrodes do not cover the entire specimen area. The apparent permittivity increases with increasing thickness, decreases with increasing area, and is much higher when the permittivity is obtained from the slope ($P$) of $1/C$ versus thickness than the slope ($Q$) of $C$ versus area ($C$ = measured capacitance). Using $P$, the value (2 kHz) for various areas is 830–1760 and 810–1750 for plain and silica-fume cements, respectively. Using $Q$, the value for various thicknesses is only 150–375 and 144–354 for plain and silica-fume cements, respectively. When the electrodes cover the entire area, the fringing field effect is weaker, with lower relative permittivity 24–38 and 23–36 for plain and silica-fume cements, respectively.



## 1. Introduction

The electric permittivity (also known as the dielectric constant, also known as the real part of the complex permittivity) is a material property that largely governs the piezoelectric, dielectric and electric polarization behavior. The piezoelectric behavior of cement-based materials pertains to applications as sensors and actuators [1–4], thereby enabling these materials to be multifunctional structural materials (i.e., smart materials). The electric permittivity of a material is a main material property that governs the interaction of electromagnetic radiation with the material. This interaction is practically important, as it is involved in the probing of concrete with ground-penetrating radar [5] and the use of concrete for electromagnetic interference (EMI) shielding [6–8]. The electric polarization behavior is central to the dielectric behavior and affects the use of these materials in applications that exploit their electrical conductivity. This is because the polarization results in a reverse electric field in the material [9,10]. Moreover, the polarization is affected by the applied strain, thus allowing strain sensing that is based on detecting the polarization [11]. The electrical conduction behavior of cement-based materials is exploited in the applications of these materials in strain/damage sensing that is based on piezoresistivity (i.e., the effect of strain/damage on the electrical resistivity) [12–16], in addition to anti-static structural components [17], Joule-heating-based deicing [18,19], electrical grounding, and lightning protection. Moreover, the electrical conduction behavior of cement-based materials is exploited in the cathodic protection of the steel reinforcement that is embedded in concrete [20–23] and to the removal of undesirable ions (such as chloride ions) from these materials by electrochemical methods [23]. The electric permittivity of cement-based materials has received little prior attention [24,25], although it is relevant to a large variety of applications. Most of the prior work on the electric permittivity of cement-based materials concerns the change of the permittivity during the hydration process [26–29].

The real part of the relative electric permittivity is a fundamental material property (commonly referred to as the relative permittivity) that describes the dielectric behavior of a material. This behavior relates to the polarizability, i.e., the separation of the positive and negative charge centers. The permittivity is one of the key parameters that govern the electromagnetic behavior of materials. Furthermore, polarization causes the apparent electrical resistivity of a material to increase, as shown for cement-based materials [30,31]. In addition, the effect of stress on the permittivity provides a mechanism for a cement-based material to sense stress [32,33]. Materials of high permittivity are needed for

* Corresponding author.
*E-mail address:* ddlchung@buffalo.edu (D.D.L. Chung).
*URL:* http://alum.mit.edu/www/ddlchung

http://dx.doi.org/10.1016/j.compositesb.2017.05.080
1359-8368/

capacitors (relevant to energy storage), ferroelectric memory, piezoelectric sensors and actuators, pyroelectric motion detectors and electromagnetic interference (EMI) shields. Cement-based materials for EMI shielding have been reported [6–8]. On the other hand, materials of low permittivity are needed for electrical insulators in high-frequency circuit applications, as the capacitance due to the polarization causes signal propagation delay.

The relative permittivity of cement-based materials has been previously reported. Admixtures affect the relative permittivity. In particular, the relative permittivity of cement paste at 10 kHz - 1 MHz is decreased by silica fume addition (from 29 to 21 at 10 kHz) [34].

The measurement of the relative permittivity typically involves a parallel-plate capacitor configuration, with the specimen under investigation being sandwiched by electrodes [34]. The electrodes can be pressure contacts or contacts involving a conductive paste, such as silver paint. The relative permittivity $\kappa$ in the direction perpendicular to the plane of the sandwich is given by the equation

$$C_v = \varepsilon_o\ \kappa\ A/l, \tag{1}$$

where $C_v$ is the capacitance due to the volume of the specimen, $\varepsilon_o$ is the permittivity of free space ($8.85 \times 10^{-12}$ F/m), $A$ is the area of the sandwich (i.e., the area of the electrode), and $l$ is the thickness of the specimen sandwiched by the electrodes.

The fringing electric field refers to the electric field in the surrounding air immediately beyond the rim of the specimen in the parallel-plate capacitor geometry. Although the permittivity of air is lower than that of the specimen, some electric field lines emanating from the two electrodes are curved away from the electrodes so that they reach the surrounding air. The fringing field results in the measured capacitance to be higher than the expected value. This is because the fringing electric field causes the specimen area to be effectively larger than the true area. As a consequence, the measured (apparent) permittivity is higher than the true value. The thicker is the specimen, the larger is the fringing field effect. The smaller is the area of the specimen, the higher is the proportion of the additional capacitance due to the fringing field effect. Although the fringing field effect has been known for numerous decades, its quantification remains in the realm of modeling rather than the realm of measurement [35–37].

The severity of the fringing field effect increases with the permittivity of the medium in which the fringing field resides. In the prior work [34], the medium is air, which has a low relative permittivity of 1.000 [38], so the fringing field effect is small. However, if the medium is the same as the specimen material (corresponding to the configuration in which the specimen extends beyond the boundary of the sandwich), the fringing field effect is relatively large. Since the permittivity of a material is affected by defects (such as cracks), the method involving such a sandwich configuration is relevant to the use of the measured (apparent) permittivity to indicate the condition of the cement-based material immediately adjacent to the area of the sandwich. This provides a new method of sensing the condition of cement-based materials. The sensing is the subject of a separate publication. The present study addresses the effect of the fringing field on the apparent permittivity of cement-based materials. Basic information on this effect is necessary prior to the sensing ability investigation.

The sandwich involves the specimen and two specimen-electrode interfaces. The specimen volume contributes to the capacitance, due to the polarization within the specimen. Each specimen-electrode interface also contributes to the capacitance, due to interfacial-space charge at the electrode. Thus, both the specimen volume and the interfaces contribute to the measured capacitance. The quantity $C_v$ in Eq. (1) is the capacitance due to the specimen alone, with the contribution of the two interfaces to the measured capacitance excluded. Therefore, reliable determination of the permittivity requires the decoupling of the volumetric and interfacial contributions. Such decoupling was not conducted in prior work on cement-based materials [34]. In contrast, this study performs this decoupling. As a result, this study provides a more accurate determination of the permittivity.

The objectives of this study are (i) to evaluate the effect of the fringing electric field on the measured (apparent) relative permittivity of cement-based materials, with the medium around the specimen (which is sandwiched by the electrodes) being extensions of the specimen, (ii) determining the relative permittivity of cement-based materials with decoupling of the volumetric and interfacial contributions to the measured capacitance, and (iii) to advance the methodology of dielectric testing of cement-based materials. Although this paper studies plain cement paste and silica-fume cement paste, the methodology is applicable to cement-based materials in general.

## 2. Methods

### 2.1. Materials

Portland cement (Type I, ASTM C150) is used. Silica fume (Elkem Materials Inc., Pittsburgh, PA, microsilica, EMS 965, USA), if applicable, is used at 15% by mass of cement [39]; it has particle size ranging from 0.03 to 0.5 μm, with average size 0.2 μm; it contains >93 wt% $SiO_2$, <0.7 wt% $Al_2O_3$, <0.7 wt% CaO, <0.7 wt% MgO, <0.5 wt% $Fe_2O_3$, <0.4 wt% $Na_2O$, <0.9 wt% $K_2O$, and <6 wt% loss on ignition, according to the manufacturer.

The silica fume has been subjected to silane treatment in order to improve its dispersion in the cement mix [40,41]. The silane coupling agent is a 1:1 (by mass) mixture of Z-6020 ($H_2NCH_2CH_2NHCH_2CH_2CH_2Si(OCH_3)_3$, Fig. 2(a)) and Z-6040 ($OCH_2$-$CHCH_2OCH_2CH_2CH_2Si(OCH_3)_3$, Fig. 2(b)) from Dow Corning Corp. (Midland, MI). The amine group in Z-6020 serves as a catalyst for the curing of the epoxy and consequently allows the Z-6020 molecule to attach to the epoxy end of the Z-6040 molecule. The trimethylsiloxy ends of the Z-6020 and Z-6040 molecules then connect to the −OH functional group on the surface of the silica fume. The silane is dissolved in ethylacetate to form a solution with 2.0 wt% silane. Surface treatment of the silica fume is performed by immersion in the silane solution, heating to 75 °C while stirring, and then holding at 75 °C for 1.0 h, followed by filtration and drying. Subsequently, the silica fume is heated at 110 °C for 12 h [40,41].

No aggregate is used. The water/cement ratio is 0.35. A high-range water reducing agent (Glenium 3000NS, BASF Construction Chemicals) is used at 1.0% by mass of cement. The defoamer (Colloids Inc., Marietta, GA, 1010, USA) is used at 0.13% (% of specimen volume). All the ingredients are mixed in a rotary mixer with a flat beater.

Square plastic molds of dimensions 240 × 240 mm are used. For all specimens, after filling the mold, an external vibrator is used to facilitate compaction and diminish the air bubbles. The specimens are demolded after 24 h and then cured at a relative humidity of nearly 100% for 28 days. The specimen thicknesses are described in Sec. 2.3. No cracking occurs upon curing for any of the specimens in this work.

### 2.2. Decoupling the volumetric and interfacial contributions to the measured capacitance

A method of decoupling the volumetric and interfacial contributions to the measured capacitance involves testing multiple

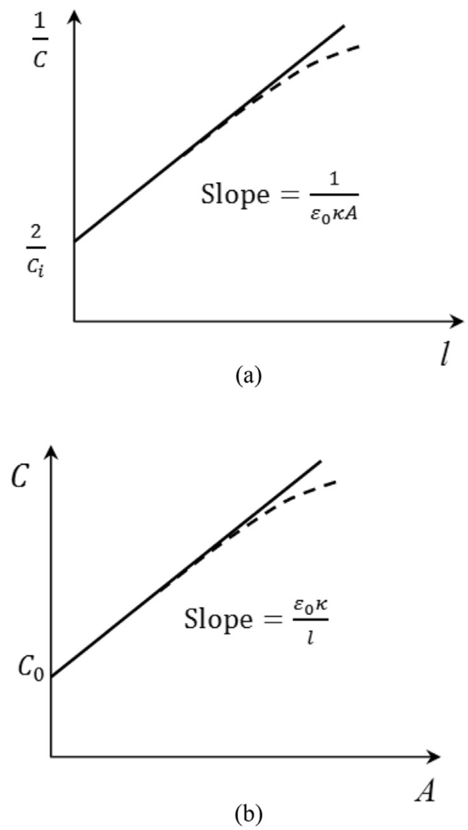


**Fig. 1.** Two methods of measuring the permittivity. (a) The method involving testing at different thicknesses and plotting $1/C$ versus thickness $l$, where $C$ is the measured capacitance. (b) The method involving testing at different areas and plotting the capacitance $C$ vs. area $A$. In both (a) and (b), the dashed curve corresponds to the case of significant fringing field effect, whereas the solid curve corresponds to the case of negligible fringing field effect.

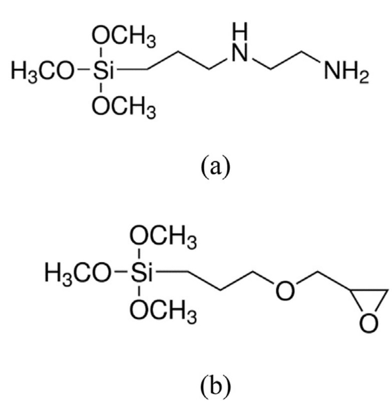


**Fig. 2.** The molecular structure of two alkylsilanes. (a) 3-(2-aminoethylamino)propyltrimethoxysilane (Z-6020) [75]. (b) 3-(glycidyloxypropyl)trimethoxysilane (Z-6040) [76].

sandwiches with different thicknesses of the specimen, but the same area, as previously used to study carbon materials [42–45] and manganese oxide [46]. Since the volumetric and interfacial capacitances are capacitances in series, the measured capacitance is given by

$$1/C = 2/C_i + 1/C_v. \qquad (2)$$

The factor of 2 in Eq. (2) is due to the presence of two interfaces on the two sides of the specimen. Due to Eq. (2), $C_i$ is less influential when it is large. The $C_v$ is given by Eq. (1). Due to Eqs. (1) and (2), the plot of $1/C$ against $l$ (Fig. 1(a)) is a straight line with the intercept of $2/C_i$ at the $1/C$ axis at $l = 0$, and the value of $\kappa$ is obtained from the slope, which is equal to $1/(\varepsilon_o \kappa A)$. The larger is $l$, the more is the fringing field effect, the higher is $C$, the smaller is $1/C$, the smaller is the slope, and the larger is $\kappa$.

Another method of decoupling involves testing multiple sandwiches with different areas, but the same thickness. Since the different parts of the area are capacitances in parallel, the measured capacitance $C$ is given by

$$C = C_o + \varepsilon_o\ \kappa\ A/l, \qquad (3)$$

where $C_o$ is the capacitance at $A = 0$ and relates to the fringing field effect, as obtained by extrapolating the plot of $C$ vs. $A$ to $A = 0$ (Fig. 1(b)). The larger is $C_o$, the more influential is $C_o$. The slope of this plot is equal to $\varepsilon_o\ \kappa/l$. Thus,$\kappa$ is obtained from the slope. Since the interface is structural identical for all areas, the slope effectively removes the interfacial contribution. The larger is $A$, the smaller is the fringing field effect, the smaller is $C$, the smaller is the slope and the smaller is $\kappa$.

### 2.3. Permittivity measurement

The permittivity is measured using the parallel-plate capacitor geometry, with two electrodes sandwiching the specimen symmetrically. Two testing configurations are used. In one configuration, the electrodes do not cover the entire area of the specimen (Fig. 3(a)). In the other configuration, the electrodes cover the entire area of the specimen (Fig. 3(b)).

#### 2.3.1. Configuration I

Configuration I has the electrodes not covering the entire area of the specimen. The apparent relative permittivity is obtained by using two methods, which correspond to Eqs. (2) and (3). In the method corresponding to Eq. (2), the capacitance is measured for three specimen thicknesses for each type of material and the same electrode area, such that this is conducted for each of four electrode areas (25 × 25, 50 × 50, 75 × 75 and 100 × 100 mm), which are all centered at the center of the slab (Fig. 4).

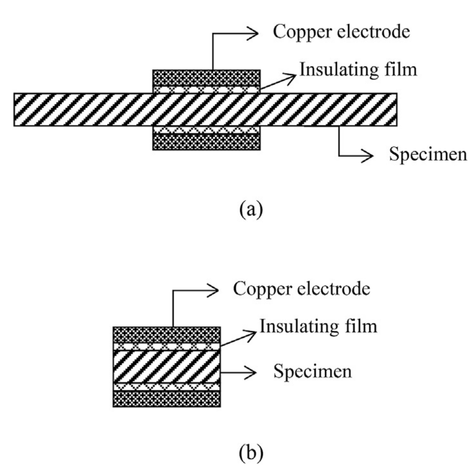


**Fig. 3.** Schematic illustration of the two testing configurations. (a) Configuration I (with the electrodes not covering the entire area of the specimen). (b) Configuration II (with the electrodes covering the entire area of the specimen).

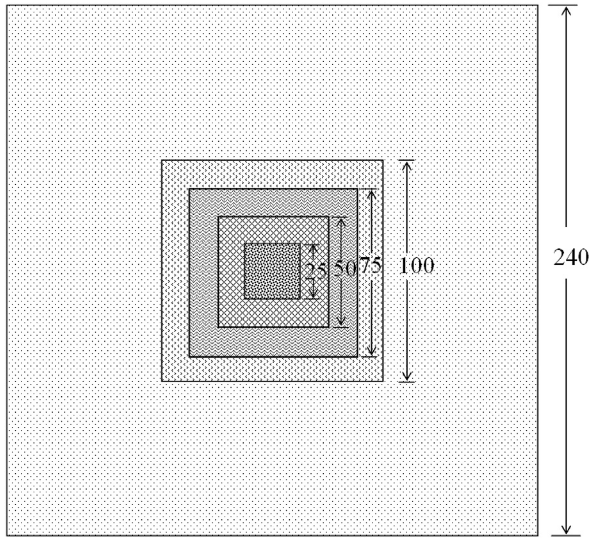


**Fig. 4.** Schematic illustration of Configuration I, showing the square specimen slab with a square electrode applied to a part of the 240 × 240 mm area of the slab. Four sizes of the electrode (each being square in shape) are used separately. For each of the four sizes, the center of the area of the electrode is positioned at the center of the area of the slab. All dimensions are in mm.

In the method corresponding to Eq. (3), the capacitance is measured for four electrode areas (25 × 25, 50 × 50, 75 × 75 and 100 × 100 mm) (Fig. 4) and the same thickness, such that this is conducted for each of three thicknesses, which are 8.39, 16.98 and 30.52 mm for plain cement paste (without silica fume), and 8.76, 17.03 and 30.60 mm for cement paste with silica fume.

Each electrode is a copper foil (0.15 mm thick), such that there is an electrically insulating plastic film (double-sided adhesive tape of thickness 0.06 mm and relative permittivity 1.5 at 2 kHz, as measured in this work) positioned between the specimen and each copper electrode. The electrode is identical in dimensions and material on the two sides of the specimens. No pressure is applied to the sandwich.

The capacitance is measured using a precision LCR meter (Instek LCR-816 High Precision LCR Meter, 100 Hz-2 kHz), with the electric field across the thickness of the specimen fixed at 0.040 V/mm. The voltage associated with the electric field is 0.35, 0.68 and 1.22 V for the specimen thicknesses of 8.38–8.76, 16.98–17.03 and 30.52–30.60 mm, respectively. The frequency used is 2 kHz. The use of a higher electric field of 0.060 or 0.120 V/mm made no difference to the results. The capacitance reported here is that for the equivalent electrical circuit of a capacitance and a resistance in parallel.

#### 2.3.2. Configuration II with the electrodes covering the entire area of the specimen

Configuration II has the electrodes covering the entire area of the specimen. The configuration is the same as Configuration I (Sec. 2.3.1), except that (i) both the specimen area and the electrode area are 25 × 25, 50 × 25 (corresponding to two 25 × 25 mm squares side by side) and 75 × 25 mm (corresponding to three 25 × 25 mm squares lined up in a row), (ii) the specimen thickness is 1.86–4.56 mm and 2.42–4.69 mm for plain cement paste and silica-fume cement pastes, respectively, (iii) the electric field is 0.11 V/mm, with the applied voltage for plain cement paste of thickness 1.86, 2.48, 3.71 and 4.56 mm being 0.20, 0.27, 0.40 and 0.49 V, respectively, and the applied voltage for silica-fume cement paste of thickness 2.42, 3.56, 4.04 and 4.69 mm being 0.26, 0.38, 0.43 and 0.50 V, respectively, (iv) a pressure of 9.93 kPa is applied in the direction perpendicular to the plane of the sandwich, (v) a Teflon film of thickness 0.058 mm and relative permittivity 1.5 at 2 kHz, as measured in this work, is positioned between each of the two sandwiching copper foils and the specimen, and (vi) the QuadTech 7600 LCR meter (10 Hz–2 MHz) is used in order to provide results over a wide frequency range.

## 3. Results and discussion

### 3.1. Configuration I

Figs. 5 and 6 show the results for Configuration I. The plots of $1/C$ vs. thickness for plain cement paste and silica-fume cement paste respectively. The curves are all essentially linear, indicating the essential validity of Eq. (2). For both plain cement paste (Fig. 5) and silica-fume cement paste (Fig. 6), the linearity increases with increasing area, due to the decrease in the fringing field effect with increasing area.

Figs. 7 and 8 show the plots of C vs. area for plain cement paste and silica-fume cement paste respectively. The curves are all essentially linear, indicating the essential validity of Eq. (3). For both plain cement paste (Fig. 7) and silica-fume cement paste (Fig. 8), the linearity decreases with increasing thickness, due to the increase in the fringing field effect with increasing thickness.

Table 1 shows the apparent relative permittivity, as obtained from the slope of the plot of $1/C$ vs. thickness and from the slope of the plot of $C$ vs. area. The values are much higher for the former method than the latter method, due to the larger fringing field effect associated with the thickness dependence. Regardless of the method, all values are higher than those obtained with the electrodes covering the entire area of the specimen by 1–2 orders of magnitude, as reported previously [34] and confirmed in this work (Sec. 3.2). This indicates the large effect of the fringing field when the electrodes do not cover the entire area of the specimen. Regardless of the method and dimensions, the apparent relative permittivity is lower for silica-fume cement paste than plain cement paste, as previously reported for the case of the electrodes covering the entire area of the specimen [34]. For the method involving the plot of $1/C$ vs. thickness, the apparent relative permittivity decreases with increasing area, because the fringing field effect decreases with increasing area. For the method involving the plot of $C$ vs. area, the apparent relative permittivity increases with increasing thickness, because the fringing field effect increases with increasing thickness.

### 3.2. Configuration II

Fig. 9 shows that the results for Configuration II. The plots of $1/C$ vs. thickness and $C$ vs. area, as obtained with the electrodes covering the entire area of the specimen. The plots are linear, particularly for the plots of $C$ vs. area (Fig. 9(b)). For the plots of $C$ vs. area, the linearity occurs for all the thicknesses investigated, although only the curve for the largest thickness for each type of cement paste is shown in Fig. 9(b). The higher degree of linearity in Fig. 9(b) than Fig. 9(a) is due to (i) the fringing field effect increasing with increasing thickness and (ii) the fact that the thickness is the variable in Fig. 9(a).

The high degree of linearity compared to the case of the

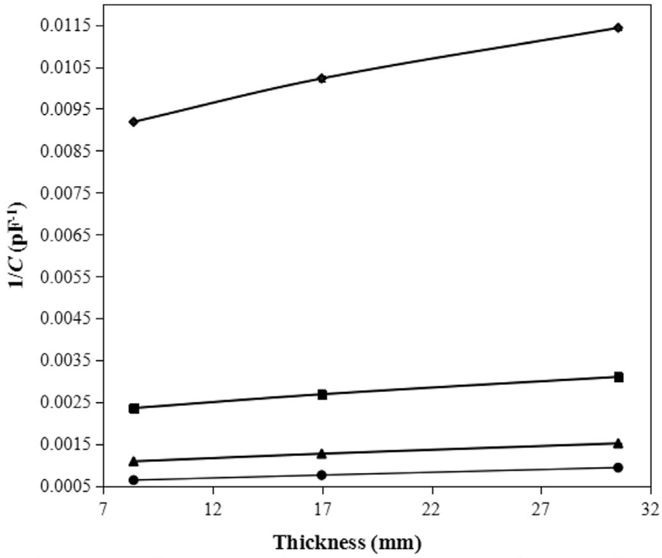


(a)

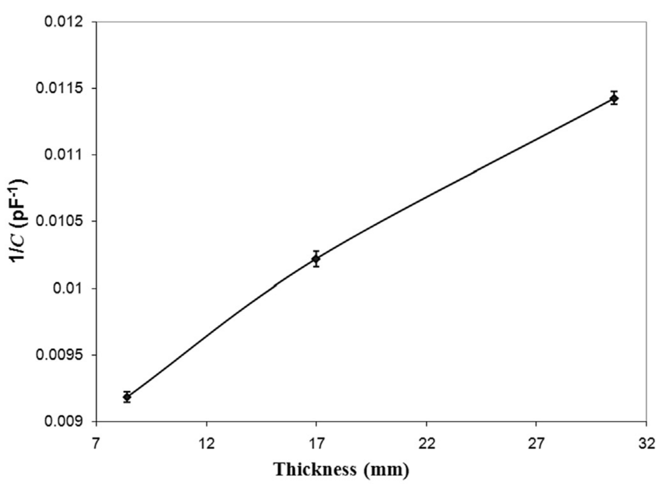


(b)

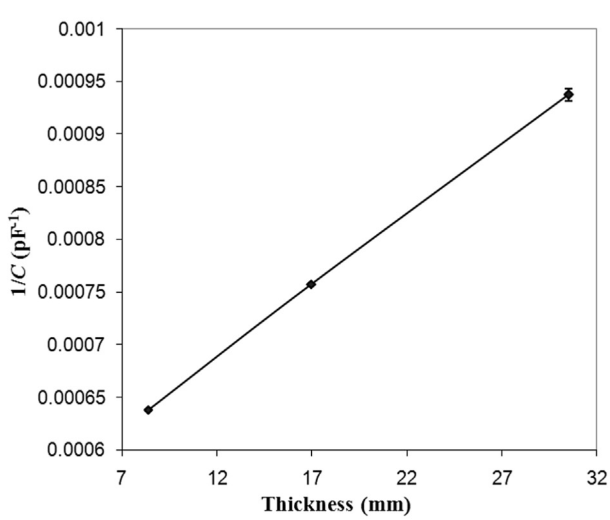


(c)

**Fig. 5.** Experimental results of plain cement paste for Configuration I, showing the plot of $1/C$ versus thickness $l$. (a) Electrode areas: ◆25 × 25 mm; ■50 × 50 mm; ▲ 75 × 75 mm; ● 100 × 100 mm. (b) The magnified view of the plot for electrode area 25 x 25 mm. (c) The magnified view of the plot for electrode area 100 x 100 mm.

electrodes not covering the entire area of the specimen (Configuration I, Sec. 3.1) is due to the weakness of the fringing field effect when the electrodes cover the entire area of the specimen. In spite of the linearity, the apparent relative permittivity, as obtained from the slope of the curve of $C$ vs. area, increases with increasing thickness (Fig. 10). This is due to the increase of the fringing field effect with increasing thickness. The most accurate value of the relative permittivity is given by the value at the smallest thickness. The apparent relative permittivity decreases with increasing frequency, as expected.

For similar small thicknesses, the apparent relative permittivity is lower for silica-fume cement paste (2.42 mm thick) than plain cement paste (2.48 mm thick). For example, at 10 Hz, the apparent relative permittivity is 28 and 25 for plain cement paste and silica-fume cement paste, respectively; at 2 MHz, the apparent relative permittivity is 18 and 12 for plain cement paste and silica-fume cement paste, respectively. The values are lower than the previously reported values [34]. In the prior work, which does not involve the decoupling of the volumetric and interfacial contributions, the relative permittivity is decreased from 24 to 17 at 1 MHz and from 29 to 21 at 10 kHz by the addition of untreated silica fume [34].

Table 2 shows that, for the case of the electrodes covering the entire area of the specimen (Configuration II) , the apparent relative permittivity is higher for the values obtained using the method of $1/C$ vs. thickness than corresponding values obtained using the method of $C$ vs. area, as for the case of the electrodes not covering the entire area of the specimen (Configuration I, Table 1). This is also shown for Configuration II by comparing Fig. 11 (method of $1/C$ vs. thickness) and Fig. 10 (method of $C$ vs. area) for frequencies ranging from 10 Hz to 2 MHz. The lower values obtained by using the latter method are more accurate, as they are closer to the previously reported values of the relative permittivity [34]. Therefore, the latter method, which has not been previously reported for any material, is more valuable than the former method, which has been previously reported for carbon and ceramic materials [40–44] (but not for cement-based materials).

The apparent relative permittivity values for plain cement paste are higher than the corresponding values for silica-fume cement paste, as shown in Tables 1 and 2 for a frequency of 2 kHz. Although Table 2 is for the frequency of 2 kHz, similarly significant differences apply to frequencies ranging from 10 Hz to 2 MHz (Configuration II, Figs. 10 and 11). The lower permittivity for silica-fume cement compared to plain cement paste is attributed to the finer pore structure in the former and the consequent greater difficulty for the ions in the pore water to move in response to the electric field. This is consistent with the reduction in the chloride ion permeability by the presence of silica fume [47].

### 3.3. Difference from the co-planar electrode configuration

Both configurations I and II of this work do not use co-planar electrodes, which are associated with a configuration in which the electric field lines spread between one electrode and the other. This spreading allows the field to penetrate selected regions for nondestructive evaluation, as shown for a glass fiber polymer-matrix composite [48].

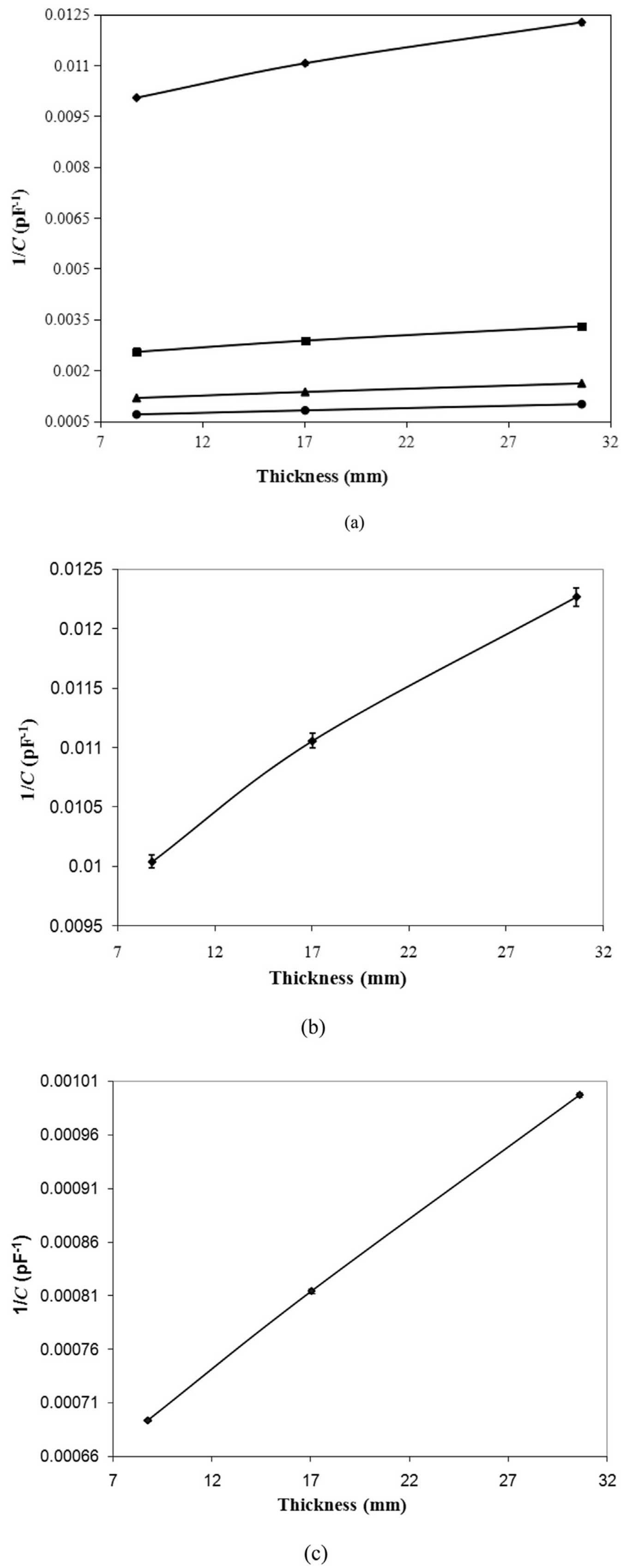


**Fig. 6.** Experimental results of silica-fume cement paste for Configuration I, showing the plot of 1/*C* versus thickness *l*. (a) Superimposed plots. Electrode areas: ◆ 25 × 25 mm; ■ 50 × 50 mm; ▲ 75 × 75 mm; ● 100 × 100 mm. (b) Magnified plot for electrode area 25 x 25 mm. (c) Magnified plot for electrode area 100 x 100 mm.

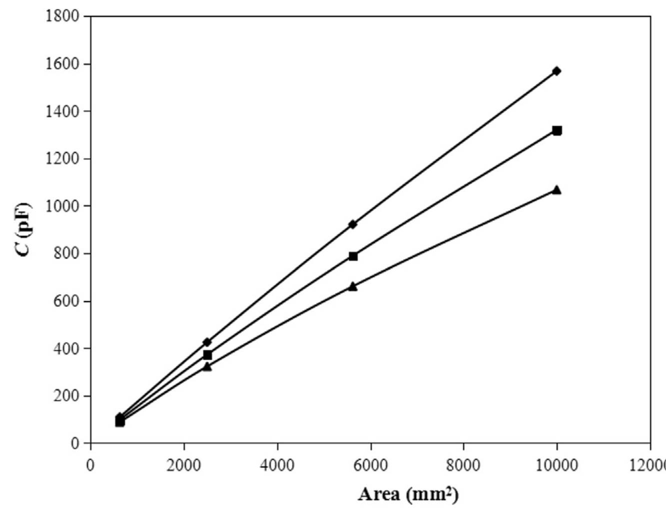


**Fig. 7.** Experimental results of plain cement paste for Configuration I, showing the superimposed plots of the measured capacitance *C* versus area *A*. Thicknesses: ◆ 8.39 mm; ■ 16.98 mm; ▲ 30.52 mm.

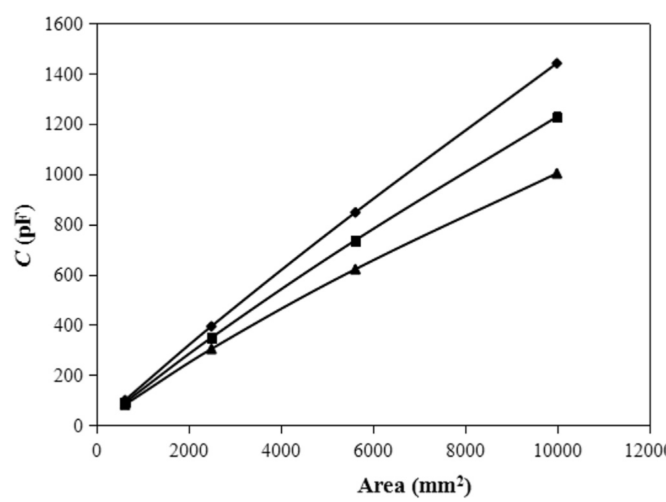


**Fig. 8.** Experimental results of silica-fume cement paste for Configuration I, showing the superimposed plots of the measured capacitance *C* versus area *A*. Thicknesses: ◆ 8.76 mm; ■ 17.03 mm; ▲ 30.60 mm.

### 3.4. Applicability to other cement-based materials

This work provides the first exposition of the fringing field effect on cement-based materials by addressing cement-based materials with and without silica fume, which is commonly used in cement-based materials. However, the technique of this work is applicable to cement-based materials in general. In particular, the application of this technique to cement pastes with polymers (e.g., latex and methylcellulose [49]) and carbons (e.g., graphite nanoplatelet [50]) is the subject of separate publications from the same research group. Due to the presence of an electrically insulating film at the interface between the specimen and an electrode, the measurement of the apparent permittivity using the method of this paper is expected to be applicable even to cement-based materials that are electrically conductive, such as those with carbon fibers [51–61], carbon nanofibers [62–64], carbon nanotubes [65–73] and

**Table 1**
Experimental results for Configuration I, showing the apparent relative permittivity of plain cement paste and silica-fume cement paste. For each type of cement paste, the results are obtained from both the slope of the plot of 1/$C$ versus thickness $l$ and the slope of the plot of $C$ versus area $A$, where $C$ is the measured capacitance. The frequency is 2 kHz.

| Material | Method of 1/C versus thickness | | | | Method of C versus area | | |
|---|---|---|---|---|---|---|---|
| | Area (mm$^2$) | | | | Thickness (mm) | | |
| | 25 × 25 | 50 × 50 | 75 × 75 | 100 × 100 | 8.39[a] 8.76[b] | 16.98[a] 17.03[b] | 30.52[a] 30.60[b] |
| Plain cement paste | 1764 ± 11 | 1327 ± 20 | 1025 ± 8 | 831 ± 15 | 150 ± 1 | 256 ± 2 | 375 ± 3 |
| Silica-fume cement paste | 1750 ± 17 | 1289 ± 9 | 1007 ± 13 | 807 ± 6 | 144 ± 1 | 240 ± 1 | 354 ± 2 |

[a] Plain cement paste.
[b] Silica-fume cement paste.

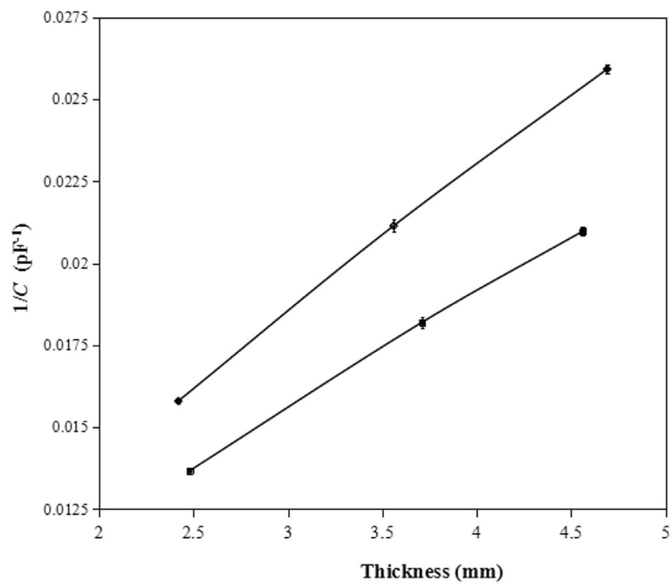


(a)

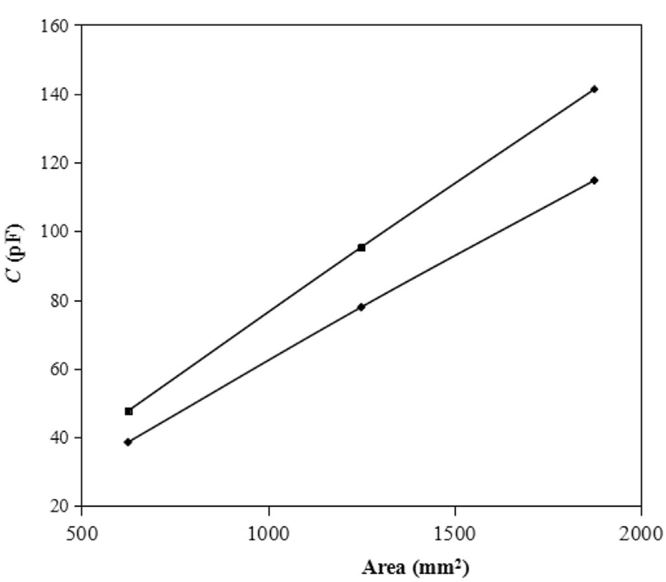


(b)

**Fig. 9.** Experimental results for Configuration II. (a) Superimposed plots of 1/$C$ versus thickness $l$. (b) Superimposed plots of $C$ versus area $A$. ■ Plain cement paste of thickness 4.56 mm ◆ Silica-fume cement paste of thickness 4.69 mm.

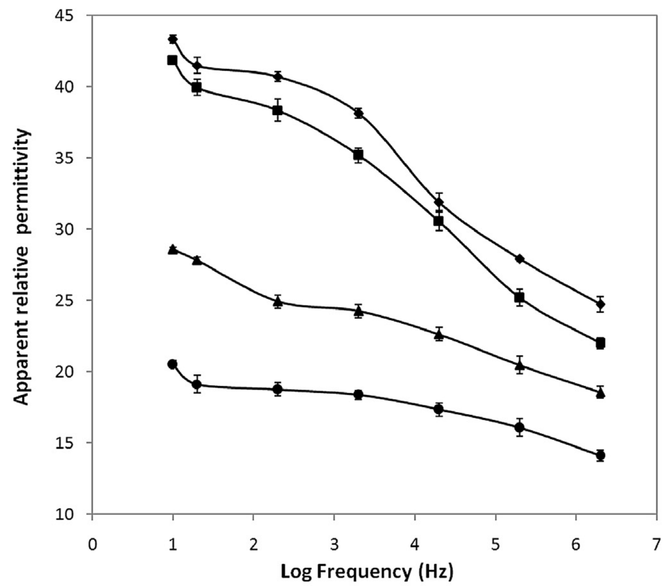


(a)

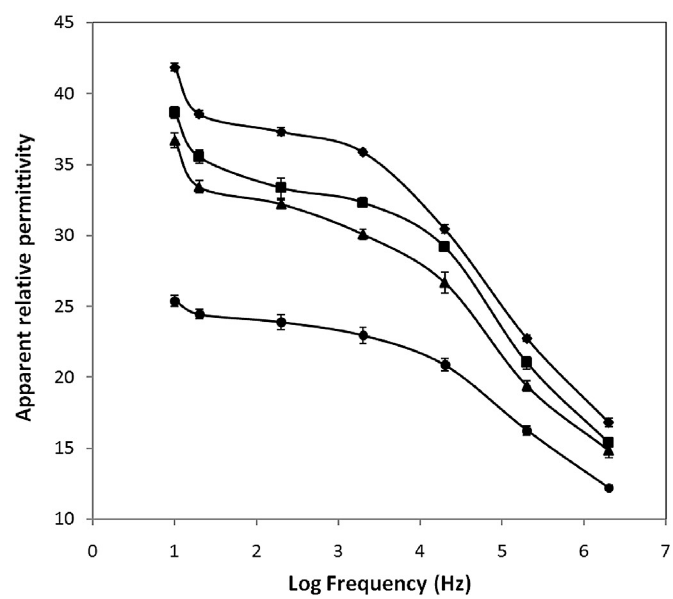


(b)

**Fig. 10.** Effects of thickness and frequency on the apparent relative permittivity obtained from plots of $C$ versus area $A$ and Configuration II. (a) Plain cement paste of thickness 1.86 mm (●), 2.48 mm (▲), 3.71 mm (■), and 4.56 mm (◆). (b) Silica-fume cement paste of thickness 2.42 mm (●), 3.56 mm (▲), 4.04 mm (■), and 4.69 mm (◆). In both (a) and (b), the apparent relative permittivity increases monotonically with increasing thickness and decreases with increasing frequency.

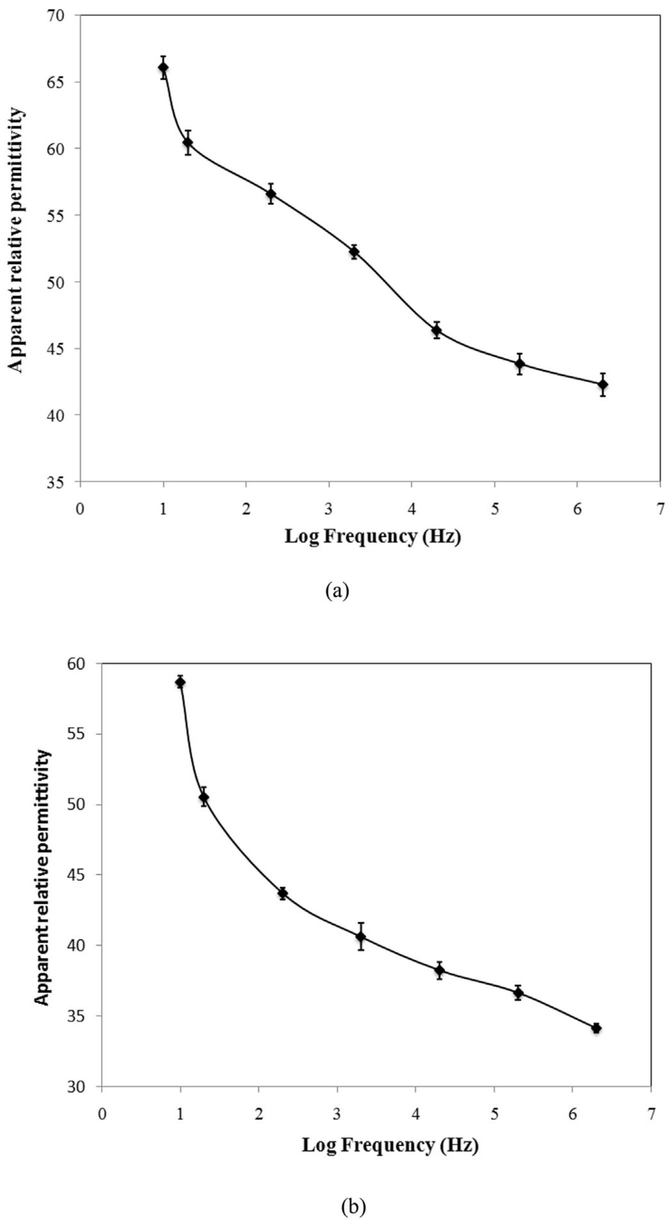


**Fig. 11.** The apparent relative permittivity obtained from the plots of $1/C$ vs. thickness $l$ for Configuration II and various frequencies, with specimen area 25 × 25 mm. (a) Plain cement paste. (b) Silica-fume cement paste.

graphite nanoplatelet [74]. This expectation is supported by the feasibility of measuring the permittivity of carbon materials in the absence of cement [42–45].

## 4. Conclusions

The fringing field effect on the apparent relative permittivity of cement-based materials is unusually strong when the electrodes do not cover the entire area of the specimen (i.e., Configuration I). This effect greatly increases the apparent relative permittivity, which increases with increasing thickness, decreases with increasing area, and is higher for the case in which the apparent relatively permittivity is obtained from the slope of the curve of $1/C$ versus thickness than the case in which the apparent permittivity is obtained from the slope of the curve of $C$ versus area. Based on the curve of $1/C$ versus thickness, the value at 2 kHz obtained for various areas is in the range from 830 to 1760 and the range from 810 to 1750 for plain cement paste and silica-fume cement paste, respectively. Based on the curve of $C$ versus area, the value at 2 kHz obtained for various thicknesses is in the range from 150 to 375 and the range from 144 to 354 for plain cement paste and silica-fume cement paste, respectively.

Configuration II (with the electrodes covering the entire area of the specimen), gives a much weaker fringing field effect than Configuration I. This is due to the low permittivity of air compared to cement. Nevertheless, with Configuration II, the fringing field effect still causes the apparent relative permittivity to increase with increasing thickness, with values ranging from 24 to 38 at 2 kHz for plain cement paste and values ranging from 23 to 36 at 2 kHz for silica-fume cement paste. These values are all much lower than the values obtained with Configuration I.

With Configuration II, the apparent relative permittivity is higher for the values obtained using the method involving the plot of $1/C$ versus thickness than the corresponding values obtained using the method involving the plot of $C$ vs. area, such that the latter values are close to the true values of the relative permittivity. Therefore, the latter method, which has not been previously reported for any material, is more valuable than the former method, which has been previously reported for carbon and ceramic materials [42–46] (but not for cement-based materials). Thus, this study advances the methodology of dielectric testing of cement-based materials.

The very high value of the apparent relative permittivity of cement pastes in case of Configuration I is expected to enable the apparent relative permittivity to be an indicator of the condition of the area of a cement-based material slab in the immediate vicinity of the electrodes sandwiching a part of the slab.

**Table 2**
Experimental results for Configuration II, showing the apparent relative permittivity of plain cement paste and silica-fume cement paste. For each type of cement paste, the results are obtained from both the slope of the plot of $1/C$ versus thickness $l$ and the slope of the plot of $C$ versus area $A$, where $C$ is the measured capacitance. The frequency is 2 kHz.

| Material | Method of $1/C$ versus thickness | Method of $C$ versus area | | |
|---|---|---|---|---|
| | Area ($mm^2$) | Thickness (mm) | | |
| | 25 × 25 | 2.48[a]<br>2.42[b] | 3.71[a]<br>3.56[b] | 4.56[a]<br>4.69[b] |
| Plain cement paste | 52.2 ± 0.5 | 24.3 ± 0.5 | 35.2 ± 0.5 | 38.1 ± 0.3 |
| Silica-fume cement paste | 40.7 ± 0.9 | 22.9 ± 0.6 | 30.1 ± 0.4 | 35.9 ± 0.2 |

[a] Plain cement paste.
[b] Silica-fume cement paste.

## Acknowledgement

The authors thank the Education Department of Fujian Province and Wuyi University for financial support of the first author (Wang).

## References

[1] Ramam K, Chandramouli K. Piezoelectric cement composite for structural health monitoring. Adv Cem Res 2012;24:165–71.
[2] Shen B, Yang X, Li Z. A cement-based piezoelectric sensor for civil engineering structure. Mater Struct Dordr Neth 2006;39:37–42.
[3] Lam KH, Chan HLW. Piezoelectric cement-based 1-3 composites. Appl Phys A-Mater 2005;81:1451–4.
[4] Zhang D, Li Z, Wu K. 2-2 Piezoelectric cement matrix composite: Part II. Actuator effect. Cem Concr Res 2002;32:825–30.
[5] Van Den Bril K, Gregoire C, Swennen R, Lambot S. Ground-penetrating radar as a tool to detect rock heterogeneities (channels, cemented layers and fractures) in the Luxembourg Sandstone Formation (Grand-Duchy of Luxembourg). Sedimentology 2007;54:949–67.
[6] Muthusamy S, Chung DDL. Carbon fiber cement-based materials for electromagnetic interference shielding. ACI Mater J 2010;107:602–10.
[7] Cao J, Chung DDL. Use of fly ash as an admixture for electromagnetic interference shielding. Cem Concr Res 2004;34:1889–92.
[8] Wen S, Chung DDL. Electromagnetic interference shielding reaching 70 dB in steel fiber cement. Cem Concr Res 2004;34:329–32.
[9] Cao J, Chung DDL. Electric polarization and depolarization in cement-based materials, studied by apparent electrical resistance measurement. Cem Concr Res 2004;34:481–5.
[10] Wen S, Chung DDL. Electric polarization in carbon fiber reinforced cement. Cem Concr Res 2001;31:141–7.
[11] Wen S, Chung DDL. Effect of stress on the electric polarization in cement. Cem Concr Res 2001;31:291–5.
[12] Wen S, Chung DDL. Piezoresistivity-based strain sensing in carbon fiber reinforced cement. ACI Mater J 2007;104:171–9.
[13] Zhu S, Chung DDL. Theory of piezoresistivity for strain sensing in carbon fiber reinforced cement under flexure. J Mater Sci 2007;42:6222–33.
[14] Wen S, Chung DDL. A comparative study of steel- and carbon-fiber cement as piezoresistive strain sensors. Adv Cem Res 2003;15:119–28.
[15] Chung DDL. Piezoresistive cement-based materials for strain sensing. J Intel Mat Syst Str 2002;13:599–609.
[16] Vipulanandan C, Mohammed A. Smart cement rheological and piezoresistive behavior for oil well applications. J Pet Sci Eng 2015;135:50–8.
[17] Shalaby A, Ward A, Refaee A, Abd-El-Messieh S, Abd-El-Nour K, El-Nashar D, et al. Compressive strength and electrical properties of cement paste utilizing waste polyethylene terephthalate bottles. J Appl Sci Ress 2013;9:4160–73.
[18] Chang C, Ho M, Song G, Mo Y, Li H. A feasibility study of self-heating concrete utilizing carbon nanofiber heating elements. Smart Mater Struct 2009;18:127001/1–127001/5.
[19] Wang S, Wen S, Chung DDL. Resistance heating using electrically conductive cements. Adv Cem Res 2004;16:161–6.
[20] Hou J, Chung DDL. Cathodic protection of steel reinforced concrete facilitated by using carbon fiber reinforced mortar or concrete. Cem Concr Res 1997;27:649–56.
[21] Aperador W, Bautista-Ruiz J, Chunga K. Determination of the efficiency of cathodic protection applied to alternative concrete subjected to carbonation and chloride attack. Int J Electrochem 2015;10:7073–82.
[22] Jeong J. Cathodic prevention and cathodic protection of concrete slab with zinc sacrificial anode. Appl Mech Mater 2014;597:341–4.
[23] Carmona J, Garces P, Climent MA. Efficiency of a conductive cement-based anodic system for the application of cathodic protection, cathodic prevention and electrochemical chloride extraction to control corrosion in reinforced concrete structures. Corros Sci 2015;96:102–11.
[24] Wen S, Chung DDL. Effect of admixtures on the dielectric constant of cement paste. Cem Concr Res 2001;31:673–7.
[25] Sachdev VK, Sharma SK, Bhattacharya S, Patel K, Mehra NC, Gupta V, et al. Electromagnetic shielding performance of graphite in cement matrix for applied application. Adv Mater Lett 2015;6:965–72.
[26] Makul N. Dielectric permittivity of various cement-based materials during the first 24 hours hydration. Open J Inorg Non-Metallic Mater 2013;3:53–7.
[27] Simon D, Grabinsky MW. Electromagnetic wave-based measurement techniques to study the role of Portland cement hydration in cemented paste backfill materials. Int J Min Reclam Env 2012;26:3–28.
[28] Tsonos C, Stavrakas I, Anastasiadis C, Kyriazopoulos A, Kanapitsas A, Triantis D. Probing the microstructure of cement mortars through dielectric parameters' variation. J Phys Chem Solids 2009;70:576–83.
[29] Abe Y, Asano M, Kita R, Shinyashiki N, Yagihara S. Dielectric study on molecular dynamics in cement hydration. Trans Mater Res Soc Jpn 2008;33:447–50.
[30] Wen S, Chung DDL. Electric polarization in carbon fiber reinforced cement. Cem Concr Res 2001;31(2):141–7.
[31] Cao J, Chung DDL. Electric polarization and depolarization in cement-based materials, studied by apparent electrical resistance measurement. Cem Concr Res 2004;34(3):481–5.
[32] Wen S, Chung DDL. Effect of stress on the electric polarization in cement. Cem Concr Res 2001;31(2):291–5.
[33] Wen S, Chung DDL. Cement-based materials for stress sensing by dielectric measurement. Cem Concr Res 2002;32(9):1429–33.
[34] Wen S, Chung DDL. Effect of admixtures on the dielectric constant of cement paste. Cem Concr Res 2001;31(4):673–7.
[35] Hosseini M, Zhu G, Peter Y. A new formulation of fringing capacitance and its application to the control of parallel-plate electrostatic micro actuators. Analog Integr Circ Sig Process 2007;53:119–28.
[36] Hosseini M, Zhu G, Peter Y. A new model of fringing capacitance and its application to the control of parallel-plate electrostatic micro actuators. Stresa, Italy: DTIP of MEMS & MOEM; April 26-28, 2006.
[37] Hegg MC, Mamishev AV. Influence of variable plate separation on fringing electric fields in parallel-plate capacitors. Conf. Rec. of 2004 IEEE Int Symp Electrical Insulation, Indianapolis, IN, USA, Sept. 19-22, 2004, pp. 384–387.
[38] http://www.engineeringtoolbox.com/relative-permittivity-d_1660.html (Accessed 11 February 2017).
[39] Cao J, Chung DDL. Microstructural effect of the shrinkage of cement-based materials during hydration, as indicated by electrical resistivity measurement. Cem Concr Res 2004;34(10):1893–7.
[40] Xu Y, Chung DDL. Improving silica fume cement by using silane. Cem Concr Res 2000;30(8):1305–11.
[41] Xu Y, Chung DDL. Cement-based materials improved by surface treated admixtures. ACI Mater J 2000;97(3):333–42.
[42] Wang A, Chung DDL. Dielectric and electrical conduction behavior of carbon paste electrochemical electrodes, with decoupling of carbon, electrolyte and interface contributions. Carbon 2014;72:135–51.
[43] Hong X, Yu W, Wang A, Chung DDL. Graphite oxide paper as a polarizable electrical conductor in the through-thickness direction. Carbon 2016;109:874–82.
[44] Hong X, Yu W, Chung DDL. Electric permittivity of reduced graphite oxide. Carbon 2017;111:182–90.
[45] Hong X, Chung DDL. Exfoliated graphite with relative dielectric constant reaching 360, obtained by exfoliation of acid-intercalated graphite flakes without subsequent removal of the residual acidity. Carbon 2015;91:1–10.
[46] Moalleminejad M, Chung DDL. Dielectric constant and electrical conductivity of carbon black as an electrically conductive additive in a manganese-dioxide electrochemical electrode, and their dependence on electrolyte permeation. Carbon 2015;91:76–87.
[47] Chung DDL. Improving cement-based materials by using silica fume. J Mater Sci 2002;37(4):673–82.
[48] Yin X, Hutchins DA. Non-destructive evaluation of composite materials using a capacitive imaging technique. Compos Part B 2012;43(3):1282–92.
[49] Wang M, Chung DDL. Understanding the increase of the electric permittivity of cement caused by latex addition. Composites, Part B, submitted.
[50] Haddad AS, Chung DDL. Decreasing the electric permittivity of cement by graphite particle incorporation. Carbon, submitted.
[51] Chung DDL. Carbon composites. second ed. Elsevier; 2016. Chapter 6.
[52] Hambach M, Moeller H, Neumann T, Volkmer D. Carbon fibre reinforced cement-based composites as smart floor heating materials. Compos Part B 2016;90:465–70.
[53] Han B, Zhang L, Zhang C, Wang Y, Yu X, Ou J. Reinforcement effect and mechanism of carbon fibers to mechanical and electrically conductive properties of cement-based materials. Constr Build Mater 2016;125:479–89.
[54] Hambach M, Moeller H, Neumann T, Volkmer D. Portland cement paste with aligned carbon fibers exhibiting exceptionally high flexural strength (> 100 MPa). Cem Concr Res 2016;89:80–6.
[55] Wei J, Zhang Q, Zhao L, Hao L, Yang C. Enhanced thermoelectric properties of carbon fiber reinforced cement composites. Ceram Int 2016;42(10):11568–73.
[56] Nevsky A, Kudyakov K, Danke I, Kudyakov A, Kudyakov V. Improvement of cement concrete strength properties by carbon fiber additives. AIP Conf Proc 2016;1698(1, Advanced Materials in Technology and Construction);070005/1-070005/5.
[57] Pellegrini Cervantes MJ, Barrios Durstewitz CP, Nunez Jaquez RE, Almeraya Calderon F, Rodriguez Rodriguez M, Castorena Gonzalez JH, et al. Conductive cement pastes with carbon fibers as anodes in the electrochemical chloride extraction. Int J Electrochem Sci 2015;10(5):3830–40.
[58] Han T, Wang H, Jin X, Yang J, Lei Y, Yang F, et al. Multiscale carbon nanosphere-carbon fiber reinforcement for cement-based composites with enhanced high-temperature resistance. J Mater Sci 2015;50(5):2038–48.
[59] Galao O, Baeza FJ, Zornoza E, Garces P. Self-heating function of carbon nanofiber cement pastes. Mater Construccion Madr Spain 2014;(314):64. e015/1-e015/11.
[60] Chung DDL. Cement reinforced with short carbon fibers: a multifunctional material. Compos Part B 2000;31(6–7):511–26.
[61] Xie N, Shi X, Feng D, Kuang B, Hui Li H. Percolation backbone structure analysis in electrically conductive carbon fiber reinforced cement composites. Compos Part B 2012;43(8):3270–5.
[62] Stephens C, Brown L, Sanchez F. Quantification of the re-agglomeration of carbon nanofiber aqueous dispersion in cement pastes and effect on the early age flexural response. Carbon 2016;107:482–500.
[63] Yazdani N, Mohanam V. Strength, bleeding and setting time of cement mortar

with carbon nanotubes and nanofibers. Adv Sci Eng Med 2016;8(6):490–5.
[64] Meng W, Khayat KH. Mechanical properties of ultra-high-performance concrete enhanced with graphite nanoplatelets and carbon nanofibers. Compos Part B 2016;107:113–22.
[65] Sun G, Liang R, Lu Z, Zhang J, Li Z. Mechanism of cement/carbon nanotube composites with enhanced mechanical properties achieved by interfacial strengthening. Constr Build Mater 2016;115:87–92.
[66] Yakovlev GI, Skripkiunas G, Polianskich IS, Lahayne O, Eberhardsteiner J, Urkhanova LA, et al. Modification of cement matrix using carbon nanotube dispersions and nanosilica. Procedia Eng 2017;172:1261–9.
[67] Chen SJ, Wang W, Sagoe-Crentsil K, Collins F, Zhao XL, Majumder M, et al. Distribution of carbon nanotubes in fresh ordinary Portland cement pastes: understanding from a two-phase perspective. RSC Adv 2016;6(7):5745–53.
[68] Yang H, Yu H, Zhao X. Reinforcement of the mechanical and durability performance of cement-based materials with multi-walled carbon nanotubes. J Adv Microsc Res 2014;9(2):93–6.
[69] Nasiri A, Shariaty-Niasar M, Rashidi A, Soltanian H. Preparation and application of carbon nanotube nanofluid as a reinforcement of cement slurry. Adv Cem Res 2014;26(3):177–84.
[70] Smilauer V, Hlavacek P, Padevet P. Micromechanical analysis of cement paste with carbon nanotubes. Acta Polytech 2012;52(6):22–8.
[71] Soliman EM, Kandil UF, Taha MMR. The significance of carbon nanotubes on styrene butadiene rubber (SBR) and SBR modified mortar. Mater Struct Dordr Neth 2012;45(6):803–16.
[72] Luo J, Duan Z, Zhao T, Li Q. Effect of compressive strain on the electrical resistivity of carbon nanotube cement-based composites. Key Eng Mater 2011;483(MEMS/NEMS Nano Technology):579–83.
[73] García-Macías E, D'Alessandro A, Castro-Triguero R, Pérez-Mira D, Ubertini F. Micromechanics modeling of the electrical conductivity of carbon nanotube cement-matrix composites. Compos Part B 2017;108:451–69.
[74] Le J, Du H, Sze Pang SD. Use of 2D graphene nanoplatelets (GNP) in cement composites for structural health evaluation. Compos Part B 2014;67:555–63.
[75] http://www.sigmaaldrich.com/catalog/product/aldrich/440302?lang=en&region=US, public domain.
[76] http://www.sigmaaldrich.com/catalog/product/aldrich/440167?lang=en&region=US, public domain.